J Mol Model (2015) 21:43
DOI 10.1007/s00894-015-2601-9

ORIGINAL PAPER

Theoretical investigation of the asymmetric molecular harmonic emission and the attosecond pulse generation

Li-Qiang Feng · Hang Liu

Received: 6 September 2014 / Accepted: 26 January 2015

Abstract The harmonic emission of the asymmetric charged molecule HeH^{2+} ion is theoretically investigated by solving the one-dimensional-time-dependent Schrödinger equation. Results show that the laser-induced electron transfer process between the vibrational state and the ground electronic state is responsible for the resonant peak on the harmonic spectrum, and that the two ionization pathways are behind the two identified cutoff energies. In addition, by optimizing the asymmetric harmonic emission, the generations of the ultrashort attosecond pulses are also discussed.

Keywords Isolated attosecond pulse · Laser-induced electron transfer · Molecular high-order harmonic generation · Vibrational state effect

Introduction

High-order harmonic generation (HHG) has been extensively investigated in literature [1–9] due to it being a good candidate for generating coherent attosecond (1as=10^{-18} s) pulses [1–3] and for studying atomic and molecular structures and dynamics [4, 5, 10–14]. Currently, the HHG process from atoms can be well understood by means of the well-known semi-classical 'three-step' model [15], where the electron is initially ionized from the ground state, then accelerated by the laser field, and finally returned to the ground state to recombine with the parent ion. Consequently, HHG photons are released, forming a supercontinuum with the maximum harmonic energy $E_{max}=I_p+3.17U_p$. I_p is the ionization potential and U_p is the ponderomotive energy of the free electron in the laser field ($U_p=e^2E^2/4m_e\omega^2$). However, when molecules are considered, the information in the molecular high-order harmonic generation shows a more complicated phenomenon compared with the atom cases due to its additional degrees of freedom and more complicated molecular structure [16, 17]. In particular, it can be separated into two categories: (i) the symmetric molecule [18, 19], i.e., H_2, H_2^+, etc., showing a similar harmonic characteristic as atoms; (ii) the asymmetric molecule [20–30], i.e., HeH^{2+}, HCl^+, etc., exhibiting the extra resonant peaks and the new cut-off energies [26–28]. This is because the electron prefers locating at one nucleus in asymmetric molecules and the electrons recolliding with neighboring nuclei can also occur [26–28]. For instance, by using the one dimensional-non-Born–Oppenheimer (NBO) model, Miao et al. [29, 30] theoretically investigated the asymmetric harmonic generation of the HeH^{2+} and reported six recombination channels on the harmonic emission process.

However, most of the previous theoretical investigations [20–28] on the asymmetric molecules were mostly based on the Born–Oppenheimer approximation (BOA) and disregarded coupling between electronic and nuclear wave packets. However, this coupling has been demonstrated to sufficiently affect electronic dynamics, and thus, should be included in studying coupled electron–nuclear motion [31, 32]. Therefore, a full-dimensional simulation that simultaneously considers the nuclear and electronic dynamics without BOA is preferred for more accuracy. However, it is too expensive to apply the full-dimensional calculation to do the

L.-Q. Feng (✉)
College of Science, Liaoning University of Technology, Jinzhou 121000, China
e-mail: lqfeng_lngy@126.com

L.-Q. Feng
State Key Laboratory of Molecular Reaction Dynamics, Dalian Institute of Chemical Physics Chinese Academy of Sciences, Dalian 116023, China

H. Liu
School of Chemical and Environmental Engineering, Liaoning University of Technology, Jinzhou 121000, China

Published online: 15 February 2015

investigation in the present paper. Thus, we use physical reasoning and intuition to reduce the dimensionality to a manageable scale that also retains the essential physics of the problem [33]. Thus, in this paper, we further investigated the asymmetric molecular harmonic emission of the HeH^{2+} by adopting the one dimensional (one dimensional nuclear motion and one dimensional electronic motion) non-Born–Oppenheimer (1+1D-NBO) model. Our results showed an intense resonant peak, which is blue shifted in comparison with the BOA model, and two identified cutoff energies. Further analyses showed that the blue shift resonant peak is caused by the laser-induced electron transfer between the vibrational state and the ground electronic state. While the two identified cutoff energies were caused by two different ionization pathways. Finally, by optimizing the laser parameters, an ultrashort attosecond pulse with duration of 56 as was generated.

Methods

In our simulations, the HHG spectra from HeH^{2+} can be calculated by numerically solving the 1+1D-NBO–time-dependent Schrödinger equation (TDSE) [33, 34]. In this model, the polarization direction of the laser pulse coincides with the nuclear axis of the molecular ion and with the restricted electronic motion. In the dipole approximation and length gauge, the TDSE is given by, (atomic units are used throughout this paper unless stated otherwise):

$$i\frac{\partial\psi(z,R,t)}{\partial t}=\left[-\frac{1}{2u_e}\frac{\partial^2}{\partial z^2}-\frac{1}{2u_N}\frac{\partial^2}{\partial R^2}+V(z,R)+\kappa zE(t)+\xi RE(t)\right]\psi(z,R,t), \quad (1)$$

where $\kappa=1+1/(m_a+m_b+1)$ and $\xi=(m_a-m_b)/(m_a+m_b)$ (m_a and m_b are the masses of the He^{2+} and H^+ nuclei, respectively). $V(z,R)=Z_1Z_2/R-Z_1/\sqrt{(z+R_1)^2+0.5}-Z_2/\sqrt{(z-R_2)^2+0.5}$ is the soft Coulomb potential, where $Z_1=2$ and $Z_2=1$ are the effective charges of the two nuclei, and $R_1=[m_b/(m_a+m_b)]R$ and $R_2=[m_a/(m_a+m_b)]R$ are the locations of the two nuclei. The most important features of this soft Coulomb potential are as follows: (1) it falls off like the true Coulomb potential at a large z value, and (2) the physical characteristics of this model allow realistic investigations of the behavior of HeH^{2+} ion in a laser field as previously proven [26–28]. $u_N=m_am_b/(m_a+m_b)$ and $u_e=(m_a+m_b)/(m_a+m_b+1)$ are the reduced masses of the nucleus and the electron, respectively. z and R are the electronic coordinate and the internuclear distance, respectively, which are defined by -100 a.u.$<z<100$a.u. and 0 a.u.$<R<30$ a.u. with the spatial step $\Delta z=0.2$ and $\Delta R=0.1$. The time-dependent wave function $\psi(z,R,t)$ can be propagated using the standard second-order split-operator method [35–38], with the initial wave function being $\psi_{initial}(z,R,t)=\varphi(R,t)\chi_{2p\sigma}(z,t)$, where $\varphi(R,t)$ and $\chi_{2p\sigma}(z,t)$ are the wave functions of the initial vibrational state and the electronic state, respectively. Here, because the $1s\sigma$ ground state is repulsive, the $2p\sigma$ excited state is chosen to be the initial electronic state. The laser field is expressed as:

$$E(t)=E_0\exp\left[-4\ln(2)(t-T_{total}/2)^2/\tau^2\right]\cos(\omega_0t+\phi), \quad (2)$$

where E_0, ω_0, τ, φ, and T_{total} are the amplitude, frequency, pulse duration carrier–envelope phase (CEP), and total pulse duration ($T_{total}=2.75\times\tau$) of the laser pulse. The harmonic spectrum $S(\omega)$ is obtained by Fourier transforming the time-dependent dipole acceleration a(t), as follows:

$$S(\omega)=\left|\frac{1}{\sqrt{2\pi}}\int_0^T a(t)e^{-i\omega_0t}dt\right|^2, \quad (3)$$

where a(t) can be given by means of Ehrenfest's theorem [39], as follows:

$$a(t)=\left\langle\psi(z,R,t)\left|-\frac{\partial V(z,R)}{\partial z}+E(t)\right|\psi(z,R,t)\right\rangle. \quad (4)$$

Finally, the attosecond pulse can be obtained by harmonic superposing as follows:

$$I(t)=\left|\sum_q a_qe^{iq\omega_0t}\right|^2 \quad (5)$$

where q means the order of the harmonic spectra and $a_q=\int_0^{T_{total}}a(t)e^{-iq\omega_0t}dt$.

Results and discussion

Resonance in HHG spectra

Figure 1a shows the HHG spectra from the 1+1D-NBO model (solid black line) and the BOA model with internuclear distance R=4.0 a.u. (solid red line). The laser parameters are 5 fs/800 nm, $I_0=1.0\times10^{15}$ W/cm^2, and $\varphi=0°$. The initial

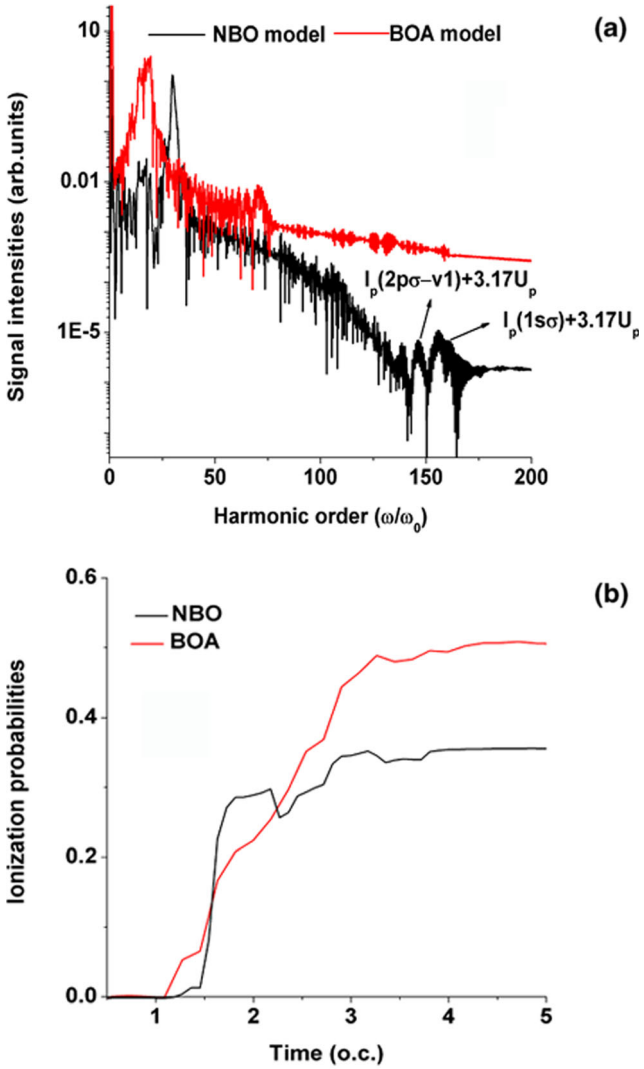

Fig. 1 (a) The HHG spectra of HeH^{2+} from the 1+1D-NBO model (*solid black line*) and the BOA model with R=4.0 a.u. (*solid red line*). The laser field is 5 fs/800 nm, $I_0=1.0\times10^{15}$ W/cm^2, and φ=0°. (b) Ionization probabilities of HeH^{2+} ion from the 1+1D-NBO model (*solid black line*) and the BOA model (*solid red line*). o.c. means the optical cycle of 800 nm pulse in all the following figures unless stated otherwise

vibrational state is chosen to be vibrational ground state (v1). It shows that the HHG spectra from the two models are quite different. In particular, (i) the harmonic yield of the BOA model is higher than that of the 1+1D-NBO model. We know that the harmonic yields are strongly dependent on the ionization probabilities [40]. Thus, in Fig. 1b, we present the ionization probabilities of the above two models. Clearly, we see that the ionization probability of the BOA model is higher than that of the 1+1D-NBO model becuase it overemphasizes the role of the atomic core, which is responsible for the different harmonic intensities of the two models. (ii) There is one resonant peak in the harmonic spectra around the 19th and 30th harmonic orders for the BOA and 1+1D-NBO models, respectively. We know that the resonant peak has been previously linked to laser-induced electron transfer process [26–28]. In particular, the electrons populated on the excited states through enhanced excitation, which may transit back to the ground state and emit photons when the laser field changes its direction, and a strong resonant peak appears around the harmonic order corresponding to the energy gap of E_{ES}–E_{GS} (E_{ES} and E_{GS} are the energies of the excited and the ground electronic states of the system). Thus, to explain the resonant peaks mentioned above, we calculate the electronic energies of the 1sσ ground and 2pσ excited states of HeH^{2+} at the internuclear distances of R=3, 4, and 5 a.u, as shown in Table 1 along with the corresponding data from ref. [41]. Through analyzing Table 1 and ref. [41], we see that the resonant position around the 19th harmonic order in the BOA model is consistent with the energy difference between the 2pσ and 1sσ states. However, for the 1+1D-NBO model, we failed to find a proper electronic state responsible for its causation. However, since we know that the NBO model contains the nuclear motion, thus, we suppose whether the blue shift resonant peak in NBO model is caused by the nuclear motion. To illuminate it, the energy of the vibrational ground state of the 2pσ state (E_{v1}=−0.528 a.u.) has been calculated. Clearly, the energy difference between the first vibrational state and the 1sσ electronic state are nearly $30\omega_0$, which is in good agreement with the position of the resonant peak in the 1+1D-NBO model. It should be illuminated that the electron transfer between the vibrational state and the ground electronic state should be occurred at arbitrary internuclear distance during the laser interaction. However, the maximum transfer probability should be around the equilibrium internuclear distance (R=4.0 a.u. for the HeH^{2+}), which is called the enhanced excitation (EE) process [42, 43]. Thus, we choose the R=3.0 a.u.-5.0.a.u. to depict the ground electronic state energy used in NBO model. Clearly, from the above analyses, the nuclear motion plays an important role in the asymmetric molecular harmonic emission. It is noted that there is another very small resonant peak around the $19\omega_0$ on the 1+1D-NBO model. We think this small peak is caused by the model limitation. Because in the 1+1D-NBO model, the HeH^{2+} becomes a three body problem, we can not separate the wave function as the single electronic state without the vibrational state (or the single vibrational state without the electronic state). Thus, we can

Table 1 Electronic energies (in a.u.) of HeH^{2+} at internuclear distances R=3, 4, and 5 a.u

R	$E_{1s\sigma}$	$E_{2p\sigma}$	$E_{2p\sigma}$–$E_{1s\sigma}$
3	−2.35 (−2.34)	−1.19 (−1.17)	$20.3\omega_0$ ($20.5\omega_0$)
4	−2.25 (−2.25)	−1.14 (−1.03)	$19.5\omega_0$ ($21.4\omega_0$)
5	−2.20 (−2.20)	−1.11 (−0.92)	$19.1\omega_0$ ($22\omega_0$)

The data in brackets are taken from ref. [41]

not explain this $19\omega_0$ resonant peak the same as the BOA model. In addition, we also can not find a proper laser-induced electron transfer vibrational state for this $19\omega_0$ resonant peak. Moreover, according to the former investigation [44], the additional virtual states in the 1D soft-core potential do have an effect on the harmonic emission. Therefore, we think the limitation of the 1D model is responsible for this small $19\omega_0$ resonant peak on the NBO model.

Cutoff energies of HHG spectra

Another interesting feature of the 1+1D-NBO HHG spectra shown in Fig. 1a is the two identified cutoff energies, that is, $E_{cutoff1}=162\omega_0$ ($I_p(1s\sigma)+3.17U_p$) and $E_{cutoff2}=132\omega_0$ ($I_p(2p\sigma\text{-}v1)+3.17U_p$). To identify and study these two harmonic emission cutoffs, in Fig. 2, we present the Coulomb potential of HeH^{2+}. We know that the $1s\sigma$ state is mainly localized on the He^{2+} ($z\leq 0$), while the $2p\sigma$ state is mainly on the H^+ ($z>0$) [26]. Due to the average lifetime of the $2p\sigma$ excited state (4 ns) [24] is significantly longer than the total pulse duration ($2.75\times\tau=13.75$ fs), thus resulting in comparable created populations (because of laser–molecule interactions) on the $1s\sigma$ ground and $2p\sigma$ excited states. Thus, the two ionization channels, which ionize from the $1s\sigma$ or $2p\sigma$ states and coexist during the ionization process, are responsible for the two identified cutoff energies.

To better understand harmonic emission process, in Fig. 3, we present the time-frequency distributions of HHG spectra, obtained by using the wavelet transformation of the dipole acceleration a(t) [45, 46]:

$$A(t,\omega_0)=\int a\left(t'\right)\sqrt{\omega_0}W\left(\omega_0\left(t'-t\right)\right)dt' \tag{6}$$

where $W(\omega_0(t'-t))$ is the Morlet wavelet with the formula of:

$$W(\xi)=\left(\frac{1}{\sqrt{\alpha}}\right)e^{i\xi}e^{-\xi^2/2\alpha^2}, \tag{7}$$

where $\alpha=30$ in our calculations. Clearly, there are many emission bursts on the harmonic emission process and each burst denotes one electronic recombination process [15]. According to Miao et al.'s results [29, 30], we know that there are six harmonic emission channels for the HeH^{2+} ion. Particularly, (i) $He^{2+}\rightarrow e\rightarrow He^{2+}$, $He^{2+}\rightarrow e\rightarrow H^+$ ionize from the nuclear He^{2+} (the 1st ionization pathway shown in Fig. 2); (ii) $H^+\rightarrow e\rightarrow H^+$, $H^+\rightarrow e\rightarrow He^{2+}$ ionize from the nuclear H^+ (the 2nd ionization pathway shown in Fig. 2); (iii) the laser-induced electron transfer between the $He\rightarrow H\rightarrow He$ and $H\rightarrow He\rightarrow H$. As illuminated before, the initial state of HeH^{2+} is prepared in the $2p\sigma$ state. Thus, the intensities of the recombination channels originating from the nucleus H^+ will be much stronger than those from the nucleus He^{2+}. Moreover, we know that the laser-induced electron transfer belongs to intermolecular transition. Thus, the emitted harmonics should be the lower orders. Now, from analyzing the time-frequency harmonic emission bursts shown in Fig. 3, we see that the bursts intensities of channels 3 and 4 are much stronger than those of channels 1 and 2. Moreover, the harmonic cutoff of channels 5 and 6 are much lower than those from the others. Therefore, we see that channels 1 and 2 are the $He^{2+}\rightarrow e\rightarrow He^{2+}$, $He^{2+}\rightarrow e\rightarrow H^+$ processes; channels 3 and 4 are the $H^+\rightarrow e\rightarrow H^+$, $H^+\rightarrow e\rightarrow He^{2+}$ processes; channels 5 and 6 are the $He\rightarrow H\rightarrow He$, $H\rightarrow He\rightarrow H$ processes, respectively. These are the main reasons behind the two identified cutoff energies and the harmonic characteristic shown in Fig. 1a.

To clearly map the electron motion between these two nuclei, the time-dependent-electron-nuclear density $|\psi(z,R,t)|^2$

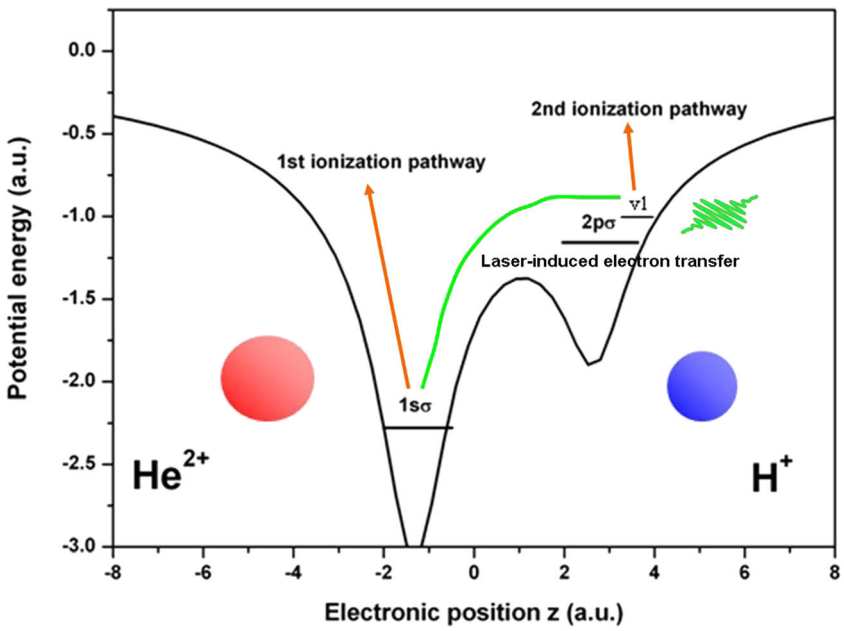

Fig. 2 A simple model for the electron transfer process

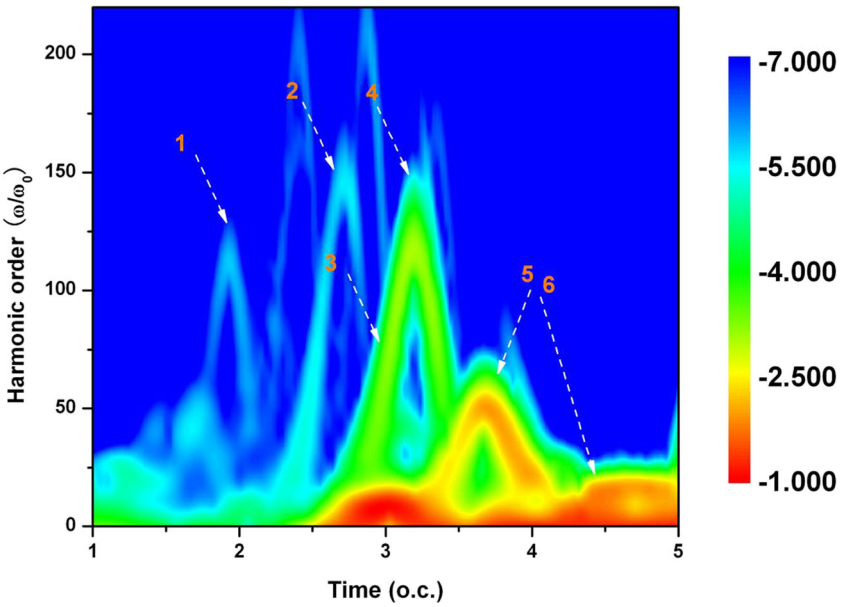

Fig. 3 Time-frequency harmonic distribution for the 1+1D-NBO model

has further been calculated at t=0, 6 fs and 10 fs, the corresponding results are shown in Figs. 4a-c. Clearly, at *t*=0, the electron is almost localized on the H^+ nucleus (z>0, Fig. 4a), and the electron begin to transfer between these two nuclei when the electronic field of the laser interacts with the molecule. In Fig. 4b and c, we can see that the electron density around the H^+ nucleus is much denser than that around the He^{2+} nucleus, which means that the probability for the electron to be ionized from the H^+ nucleus (2pσ state) is much larger than that from the He^{2+} nucleus (1sσ state).

General characteristics of the asymmetric molecule HeH^{2+}

The HHG spectra of the HeH^{2+} ion irradiated by a laser pulse with different intensities [$I_0=1.5\times10^{15}$ W/cm^2, 2.0×10^{15} W/cm^2 with $\lambda_0=800$ nm, Fig. 5a] and different wavelengths [$\lambda_0=400$ nm–700 nm with $I_0=1.0\times10^{15}$ W/cm^2, Fig. 5b] are presented in Fig. 5. All the aforementioned characteristics are found in the calculated spectra, thus indicating that these phenomena are general for the asymmetric charged molecule HeH^{2+} interacting with the normal infrared or visible laser field.

Isolated attosecond pulse generation

One of the most important applications of HHG is generating isolated attosecond pulses. Hereafter, we will discuss the generation of isolated ultrashort attosecond pulses from the asymmetric charged molecule HeH^{2+}. The laser pulse intensity is set at $I_0=2.0\times10^{15}$ W/cm^2.

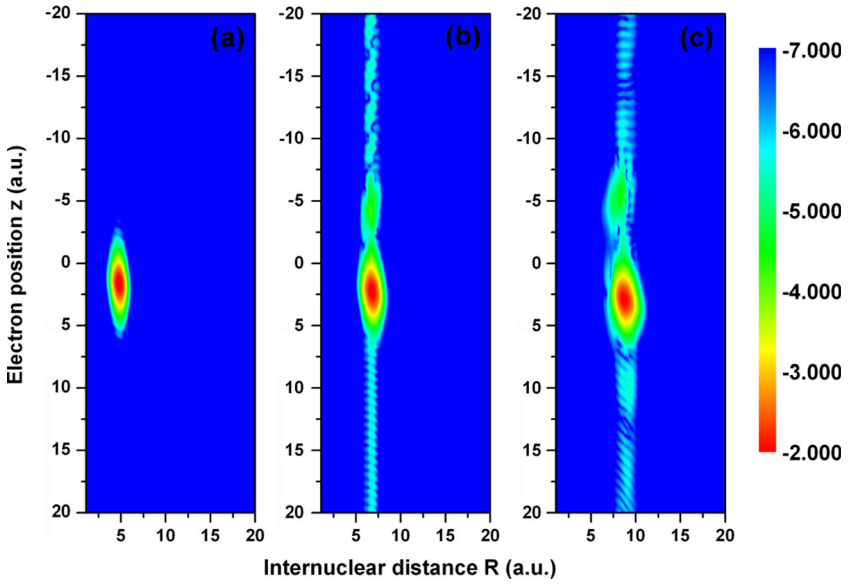

Fig. 4 The time-dependent-electron-nuclear-density at (**a**) t=0 fs, (**b**) t=6 fs, (**c**) t=10 fs

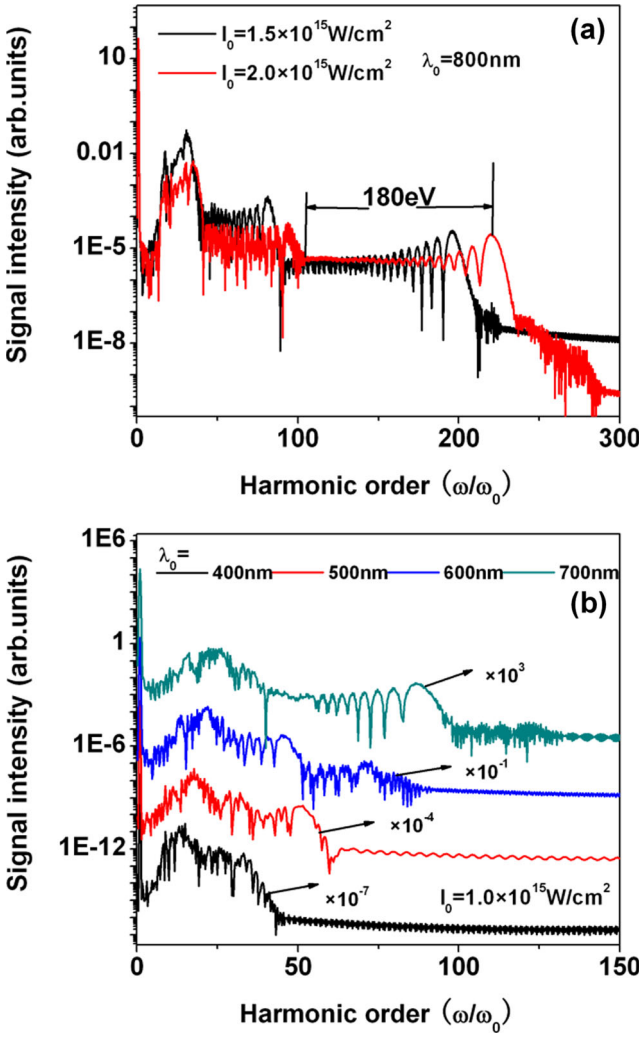

Fig. 5 (**a**) The HHG spectra of the HeH^{2+} ion from the 1+1D-NBO model at different pulse intensities of $I_0=1.5\times10^{15}$ W/cm^2 (*solid black line*) and $I_0=2.0\times10^{15}$ W/cm^2 (*solid red line*). (**b**) The HHG spectra of the HeH^{2+} ion from the 1+1D-NBO model at different wavelengths of λ_0= 400 nm (*solid black line*), 500 nm (*solid red line*), 600 nm (*solid blue line*), and 700 nm (*solid dark cyan line*). Other parameters are similar to those in Fig. 1a

Figure 6a (left column) shows the harmonic spectra as a function of the CEPs ($-180°\leq\varphi\leq180°$). Clearly, the harmonic spectra are strongly dependent on CEPs. An increase in CEP value significantly extends both the maximum (solid orange line) and second maximum (solid black line) cutoff energies. This situation is not advantageous for the formation of an ultrabroad supercontinuum (the difference between the maximum and the second maximum harmonic cutoffs). Moreover, the large modulations on the corresponding HHG spectra are also unfavorable for generating an isolated attosecond pulse. Through our calculations, we have found two proper CEPs, $\varphi=0°$ and $\varphi=60°$, which have resulted in the 178 eV and 180 eV bandwidths with less modulations as shown at the right column of Fig. 6a (the other harmonics are not shown due to the larger modulations on the harmonic plateau). Until now, the above single laser field can generate an isolated attosecond pulse. However, we know that the broader and smoother harmonic plateau we get, the shorter attosecond pulse will be obtained. Thus, to improve the attosecond generation, we use the controlling field scheme to further extend the harmonic cutoff. First, we have applied a two-color scheme in the region where the 5 fs/800 nm pulse is combined with a normal infrared field (400–2000 nm). The results are inconclusive because the large interferential structures are present in the calculated harmonic spectra (not shown in this paper). Next, we have attempted to add a static field on the 5 fs/800 nm laser field but the aforementioned interferential structures remain, which is unbeneficial to the isolated attosecond selection [47], as shown in Fig. 6b. An example is the case of ri=0.2, where ri represents the relative strength ratio between the static field and the fundamental 800 nm field. Then, we have attempted to add a chirp controlling pulse (15 fs/400 nm with $I_{control}=3.0\times10^{14}$ W/cm^2) with the chirp forms of $\delta(t)=-\beta\tanh(t/200)$. It shows that with the increasing of the chirp, the harmonic cutoff has been further extended. Especially for $\varphi=0°$, $\beta=3.0$ and $\varphi=60^o$ $\beta=1.0$ two cases, two supercontinuums with the bandwidths around 270 eV can be obtained, as shown in Fig. 6c and d (solid red lines and these are the optimal chirp parameters under the present laser field). To explain the chirp effect on the harmonic extension process, in Fig. 7a and b, we present the laser profiles of the above chirped combined fields. According to the 'three-step' model, we know that the electron is ionized around the B point and accelerated away from the ion core. Further, when the electric field inverses its direction around C point, the electron is first decelerated and then accelerated reversely. Finally, the electron can recombine with its parent ion at D point and emit a harmonic photon. From analyzing the laser profiles, we see that due to the introduced chirp, the B-C-D process has been broadened. Thus, the electron must take much more time in its processes of accelerating and returning to the parent ion, which is responsible for the extension of the cutoff energy [8].

Figure 8a-d shows the time-frequency distributions of the four cases: the single 5 fs/800 nm pulse with $I_0=2.0\times10^{15}$ W/cm^2 at (i) $\varphi=0°$ and (ii) $\varphi=60°$; and the combination of 5 fs/800 nm and 15 fs/400 nm pulses with $I_{control}=3.0\times10^{14}$ W/cm^2 at (iii) $\beta=3.0$, $\varphi=0°$ and (iv) $\beta=1.0$, $\varphi=60°$. Clearly, there are two main emission bursts on the harmonic emission and the maximum energy values are all in good agreement with the quantum results shown in Fig. 6. Moreover, each burst receives two contributions from the long quantum path (right path) having earlier ionization and later recollision and the short quantum path (left path) with later ionization but earlier recollision [48]. For the single laser field two cases (Fig. 8a and b), we see that the contribution from the short quantum path is higher than that from the long quantum path, which is responsible for the small modulations on the

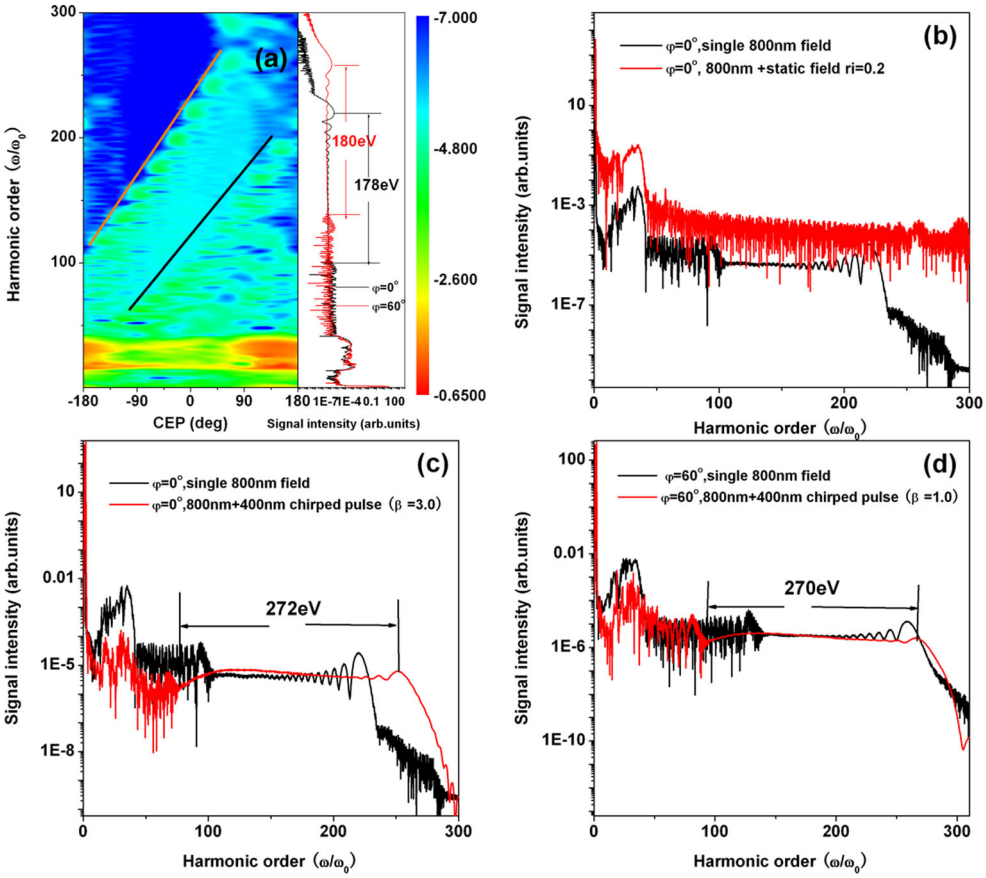

Fig. 6 (**a**) *Left column*: the HHG spectra as a function of the CEP of φ. *Right column*: the HHG spectra at two special CEP values, i.e., φ=0° (*solid black line*) and φ=60° (*solid red line*). Other parameters are the same as those in Fig. 1a. The HHG spectra for the cases of adding (**b**) a static pulse at ri=0.2 and φ=0° (*solid red line*); (**c**) a 15 fs/400 nm chirp controlling pulse with β=3.0, $I_{control}=3.0\times10^{14}$ W/cm^2, and at φ=0° (*solid red line*); and (**d**) a 15 fs/400 nm chirp controlling pulse with β=1.0, $I_{control}=3.0\times10^{14}$ W/cm^2, and at φ=60° (*solid red line*). The HHG spectra from each single laser field are also shown (*solid black line*) for comparison

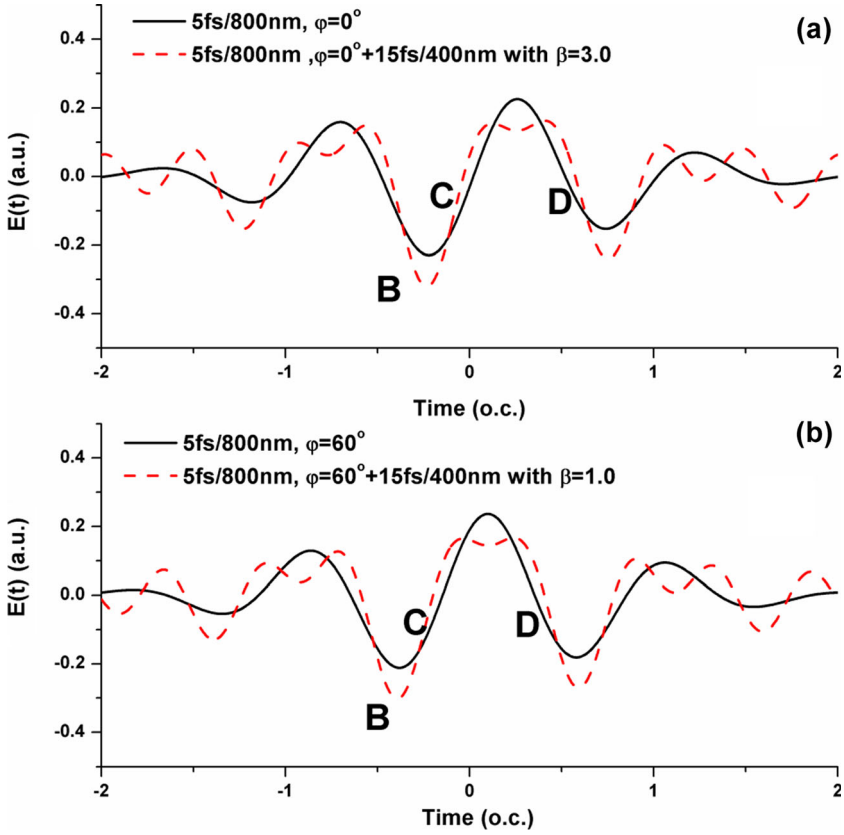

Fig. 7 (**a**) Laser profiles of the single 5 fs/800 nm, φ=0° pulse (*solid black line*) and the 5 fs/800 nm+15 fs/400 nm chirped pulse with φ=0° and β=3.0. (**b**) Laser profiles of the single 5 fs/800 nm, φ=60° pulse (*solid black line*) and the 5 fs/800 nm+15 fs/400 nm chirped pulse with φ=60° and β=1.0

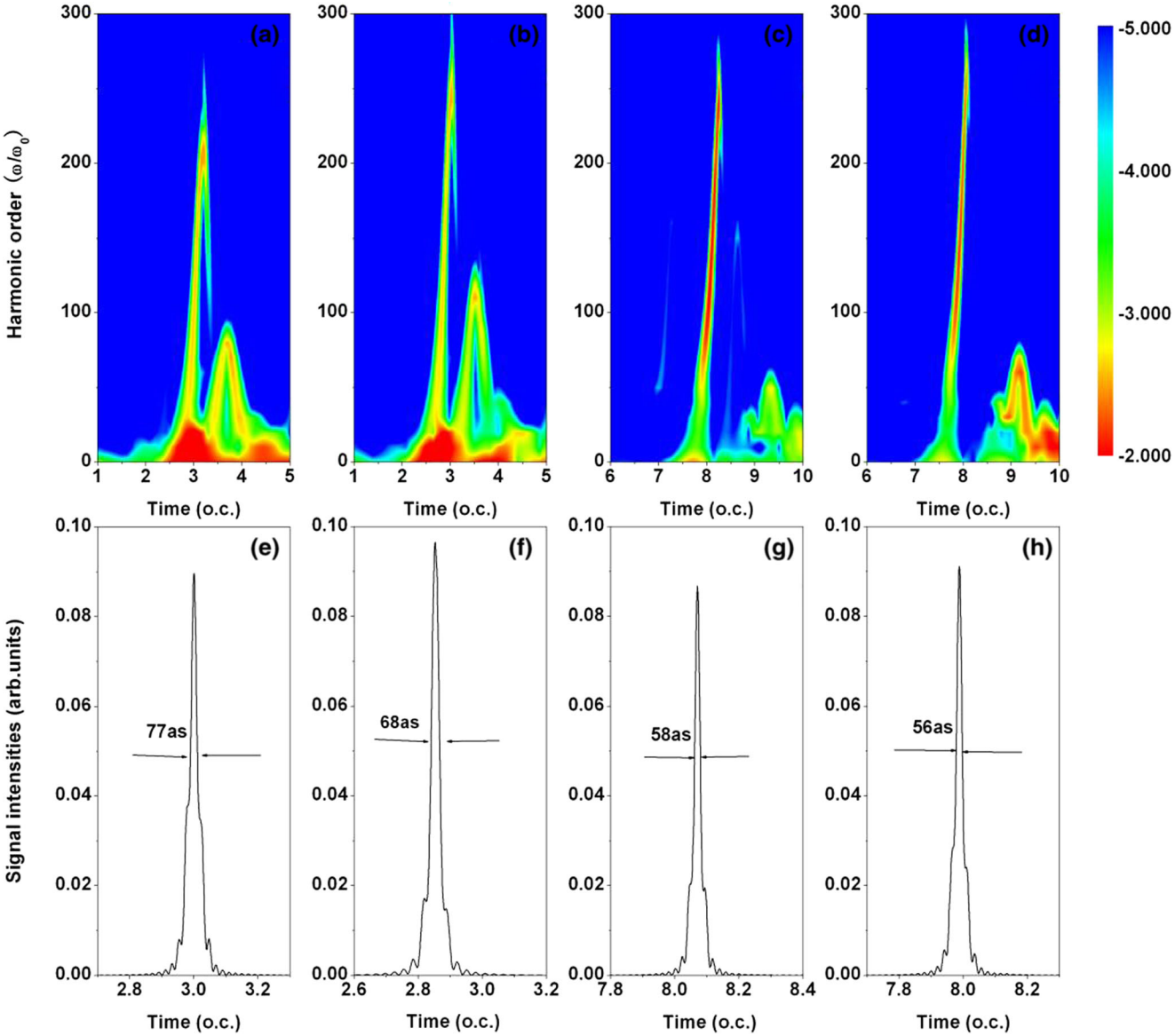

Fig. 8 (**a**)–(**d**) Time-frequency results for the four optimal cases as illustrated in the text. (**e**)–(**h**) Temporal profiles of the isolated attosecond pulses by superposing the harmonics in the aforementioned four cases

harmonic spectra shown in Fig. 6a right column. Furthermore, with the introduction of the controlling chirp pulse (Fig. 8c and d), the short quantum path is well selected to contribute to the harmonic emission, which proves to be favorable in generating an isolated ultrashort attosecond pulse.

Figure 8e-h shows the temporal profiles of the attosecond pulses. Due to the fact that the harmonics do not emit at the same time, the selection of an entire supercontinuum region no longer provides the perfect possible situation for generating an attosecond pulse [8, 49]. Therefore, by properly superposing the selected harmonics on the above harmonic spectra (that is, from the 100th to the 150th for case (i), from the 145th to the 195th for case (ii), from the 120th to the 165th for case (iii), and from the 200th to the 250th for case (iv)). Four isolated attosecond pulses as short as 77, 68, 58, and 56 as can be directly obtained, as shown in Fig. 8e-h, respectively.

Conclusions

In conclusion, by solving the 1+1D-NBO–TDSE, we have studied the asymmetric molecular harmonic emission and the attosecond pulse generation from the diatomic asymmetric charged molecule HeH^{2+}. The intense resonance peak and two identified cutoff energies are evident characteristics found in the harmonic emission process. A detailed analysis of the electronic and the vibrational energies reveal that the laser-induced electron transfer between the electronic state and the vibrational state, is responsible for the blue shift resonance

peak on the harmonic spectrum (in comparison with the BOA result). Meanwhile, the two ionization pathways and six harmonic emission channels are responsible for the two cutoff energies and the harmonic structure. Finally, by optimizing the laser parameters within the one-color and two-color schemes, we have found four optimization conditions, under which an isolated attosecond pulse, with a duration of 77 as or 68 as for the one-color scheme) and 58 as or 56 as for the two-color scheme, has been directly generated from the HHG spectra of the asymmetric molecule HeH^{2+}.

Acknowledgments The author thanks Professor Keli Han for providing the computational code used in the present work. Project supported by the Scientific Research Fund of Liaoning Provincial Education Department, China (Grant Nos. L2014242 and L2012223) and the Scientific Research Fund of Liaoning University of Technology, China (Grant Nos. X201319 and X201312).

References

1. Krausz F, Ivanov M (2009) Rev Mod Phys 81:163–234
2. Sansone G, Benedetti E, Calegari F, Vozzi C, Avaldi L, Flammini R, Poletto L, Villoresi P, Altucci C, Velotta R, Stagira S, Silvestri SD, Nisoli M (2006) Science 314:443–446
3. Goulielmakis E, Schultze M, Hofstetter M, Yakovlev VS, Gagnon J, Uiberacker M, Aquila AL, Gullikson EM, Attwood DT, Kienberger R, Krausz F, Kleineberg U (2008) Science 320:1614–1617
4. Uiberacker M, Uphues T, Schultze M, Verhoef AJ, Yakovlev V, Kling MF, Rauschenberger J, Kabachnik NM, Schröder H, Lezius M, Kompa KL, Muller HG, Vrakking MJJ, Hendel S, Kleineberg U, Heinzmann U, Drescher M, Krausz F (2007) Nature 446:627–632
5. Lein M (2005) Phys Rev Lett 94:053004
6. Sansone G, Kelkensberg F, Pérez-Torres JF, Morales F, Kling MF, Siu W, Ghafur O, Johnsson P, Swoboda M, Benedetti E, Ferrari F, Lépine F, Sanz-Vicario JL, Zherebtsov S, Znakovskaya I, L'Huillier A, Ivanov MY, Nisoli M, Martin F, Vrakking MJJ (2010) Nature 465: 763–U3
7. Chen YJ, Liu J, Hu B (2009) J Chem Phys 130:044311
8. Feng LQ, Chu TS (2011) Phys Rev A 84:053853
9. Marangos JP, Baker S, Kajumba N, Robinson JS, Tisch JWG, Torres R (2008) Phys Chem Chem Phys 10:35–48
10. Das T, Augstein BB, Figueira de Morisson Faria C (2013) Phys Rev A 88: 023404
11. Lai XY, Figueira de Morisson Faria C (2013) Phys Rev A 88: 013406
12. Yuan KJ, Bandrauk AD (2013) Phys Rev Lett 110:023003
13. Feng LQ, Chu TS (2012) J Mol Model 18:5097–5106
14. Han YC, Madsen LB (2013) Phys Rev A 87:043404
15. Corkum PB (1993) Phys Rev Lett 71:1994–1997
16. Kamta GL, Bandrauk AD (2005) Phys Rev A 71:053407
17. Figueira de Morisson Faria C (2007) Phys Rev A 76: 043407
18. Lein M, Hay N, Velotta R, Marangos JP, Knight PL (2002) Phys Rev A 66:023805
19. Yang WF, Song XH, Zeng ZN, Li RX, Xu ZZ (2010) Opt Express 18: 2558–2565
20. Lan PF, Lu PX, Li F, Li QG, Hong WY, Zhang QB, Yang ZY, Wang XB (2008) Opt Express 16:17542–17553
21. Du HC, Wang HQ, Hu BT (2011) Chin Phys B 20:044207
22. Benltzhak I, Bouhnik JP, Esry BD, Gertner I, Heber O, Rosner B (1996) Phys Rev A 54:474–479
23. Kirchner T (2002) Phys Rev Lett 89:093203
24. Itzhak IB, Gertner I, Heber O, Rosner B (1993) Phys Rev Lett 71: 1347–1350
25. Liu KL, Hong WY, Lu PX (2011) Opt Express 19:20279–20287
26. Bian XB, Bandrauk AD (2011) Phys Rev A 83:041403
27. Bian XB, Bandrauk AD (2010) Phys Rev Lett 105:093903
28. Bian XB, Bandrauk AD (2011) Phys Rev A 83:023414
29. Miao XY, Zhang CP (2014) Laser Phys Lett 11:115301
30. Miao XY, Du HN (2013) Phys Rev A 87:053403
31. Zhao J, Zhao ZX (2008) Phys Rev A 78:053414
32. Liu CD, Zeng ZN, Wei PF, Liu P, Li RX, Xu ZZ (2010) Phys Rev A 81:033426
33. He HX, Lu RF, Zhang PY, Han KL, He GZ (2012) J Chem Phys 136: 024311
34. Feng LQ, Chu TS (2012) J Chem Phys 136:054102
35. Lu RF, Zhang PY, Han KL (2008) Phys Rev E 77:066701
36. Hu J, Han KL, He GZ (2005) Phys Rev Lett 95:123001
37. Chu TS, Zhang Y, Han KL (2006) Int Rev Phys Chem 25:201–235
38. Xie TX, Zhang Y, Zhao MY, Han KL (2003) Phys Chem Chem Phys 5:2034–2038
39. Burnett K, Reed VC, Cooper J, Knight PL (1992) Phys Rev A 45: 3347–3349
40. Feng LQ, Chu TS (2012) IEEE J Quant Electron 48:1462–1466
41. Campos JA, Nascimento DL, Cavalcante DT, Fonseca ALA, Nunes AOC (2006) Int J Quantum Chem 106:2587–2596
42. Lagmago Kamta G, Bandrauk AD (2007) Phys Rev A 76:053409
43. Dehghanian E, Bandrauk AD, Lagmago Kamta G (2013) J Chem Phys 139:084315
44. Feng LQ, Chu TS (2013) Commun Comput Chem 1:52–62
45. Antoine P, Piraux B, Maquet A (1995) Phys Rev A 51:R1750–R1753
46. Feng LQ, Yuan MH, Chu TS (2013) Phys Plasmas 20:122307
47. Feng LQ, Chu TS (2012) Chem Phys 405:26–31
48. Mairesse Y, Bohan AD, Frasinski LJ, Merdji H, Dinu LC, Monchicourt P, Breger P, Kovačev M, Taïeb R, Carré B, Muller HG, Agostini P, Salières P (2003) Science 302:1540–1543
49. Feng LQ, Chu TS (2012) J Electron Spectrosc Relat Phenom 185: 458–465